Accelerated Short Circuiting in Anode-Free Solid-State Batteries Driven by Local Lithium Depletion

John A. Lewis, Stephanie E. Sandoval, Yuhgene Liu, Douglas Lars Nelson, Sun Geun Yoon, Runzi Wang, Ying Zhao, Mengkun Tian, Pavel Shevchenko, Emilio Martínez-Pañeda, Matthew T. McDowell*

John A. Lewis, Stephanie E. Sandoval, Yuhgene Liu, Douglas Lars Nelson, Matthew T. McDowell
School of Materials Science and Engineering, Georgia Institute of Technology, 771 Ferst Drive, Atlanta, GA, 30332
E-mail: mattmcdowell@gatech.edu

Sun Geun Yoon, Matthew T. McDowell
George W. Woodruff School of Mechanical Engineering, Georgia Institute of Technology, 801 Ferst Drive, Atlanta, GA, 30332

Runzi Wang, Emilio Martínez-Pañeda
Department of Civil and Environmental Engineering, Imperial College London, London SW7 2AZ, UK

Ying Zhao
School of Aerospace Engineering and Applied Mechanics, Tongji University, Shanghai 200092, China

Mengkun Tian
Institute for Electronics and Nanotechnology, Georgia Institute of Technology, Atlanta, GA, 30332, USA

Pavel Shevchenko
Advanced Photon Source, Argonne National Laboratory, Lemont, IL, USA

Abstract

"Anode-free" solid-state batteries (SSBs), which have no anode active material, can exhibit extremely high energy density (~1500 Wh L^{-1}). However, there is a lack of understanding of the lithium plating/stripping mechanisms at initially lithium-free solid-state electrolyte (SSE) interfaces, since excess lithium metal is often used. Here, we demonstrate that commercially relevant quantities of lithium (>5 mAh cm^{-2}) can be reliably plated at moderate current densities (1 mA cm^{-2}) using the sulfide SSE Li$_6$PS$_5$Cl. Investigations of lithium plating/stripping mechanisms, in conjunction with cryo-focused ion beam (FIB) imaging, synchrotron tomography, and phase-field modeling, reveal that the cycling stability of these cells is fundamentally limited by the nonuniform presence of lithium during stripping. Local lithium depletion causes isolated lithium regions toward the end of stripping, decreasing electrochemically active area and resulting in high local current densities and void formation. This accelerates subsequent filament growth and short circuiting compared to lithium-excess cells. Despite this degradation mode, we show that anode-free cells exhibit comparable Coulombic efficiency to lithium-excess cells, and improved resistance to short circuiting is achieved by avoiding local lithium depletion through retention of thicker lithium at the interface. These new insights provide a foundation for engineering future high-energy anode-free SSBs.

1. Introduction

Solid-state batteries (SSBs) could provide higher energy density than conventional lithium-ion batteries by enabling the use of the lithium metal anode.[1–5] Lithium metal SSBs with "anode-free" architectures have recently attracted attention due to the advantages of eliminating excess lithium metal (Figure 1a).[6,7] In an anode-free SSB, the cell is initially assembled without active material at the anode, and the anode is formed *in situ* by plating lithium pre-stored in the cathode.[6–11] Key advantages are the reduction in cell stack volume by ~15%, resulting in a large increase in energy density (Figure 1a), as well as the removal of the need to handle air-sensitive lithium metal in a manufacturing environment.[7,11] Anode-free SSB architectures could therefore increase energy density while also simplifying manufacturing and lowering cell costs.

While there is great interest in anode-free SSBs,[6,7] achieving stable cycling in these cells is challenging.[12,13] One reason is that it is difficult to create uniform physical contact between the solid-state electrolyte (SSE) and metal current collectors to enable initial lithium plating at high current densities, in contrast to soft lithium metal which can deform to contact the SSE. Poor interfacial contact will increase the local current density in some regions,[14–17] promoting the growth of lithium filaments that can short circuit the cell.[18–22] Additionally, the Coulombic efficiency (CE) of anode-free cells must be very high since there is no excess lithium to compensate for lithium loss due to side reactions. Lithium metal anodes in both SSBs and liquid electrolytes have been observed to exhibit relatively low CEs,[23,24] making this challenge difficult to solve. Designing viable anode-free SSBs therefore requires a detailed understanding of contact evolution, lithium filament growth, and capacity retention during plating and stripping at current collector/SSE interfaces.

Despite growing interest, there has been relatively little work studying the mechanisms of plating and stripping in anode-free SSBs. Some studies have plated and stripped lithium on current collectors to measure Coulombic efficiency,[25–27] but they did not investigate

3

underlying mechanisms at these interfaces. Anode-free cells have also been used to observe lithium electrodeposition,[28–32] but these configurations were generally chosen to avoid the challenges of probing buried interfaces. Recently, Wang *et al.* demonstrated that ≥ 3 mAh cm^{-2} of Li could be cycled at interfaces between current collectors and the garnet $Li_7La_3Zr_2O_{12}$ (LLZO) SSE.[12] However, these cells operated at relatively low current densities (≤ 0.3 mA cm^{-2}) and required hot pressing of current collectors onto LLZO at temperatures > 900 °C. Further work has demonstrated void formation during stripping, as well dependence of stripping mechanisms on lithium thickness.[33] Other work has investigated anode-free SSBs using the softer Li_6PS_5Cl (LPSC) SSE,[13] finding that performance was limited by the poor deposition morphology of lithium at intrinsic current collector interfaces. This led to the approach of incorporating a Ag-C layer between the current collector and SSE, which facilitated uniform deposition. Although these cells exhibited excellent performance,[13] the mediator layers reduce energy density. Despite these advances, much is still unknown about how the plating and stripping mechanisms at interfaces with zero initial lithium metal differ from interfaces with excess lithium metal, which are much more commonly studied.

Here, we investigate the mechanisms of plating and stripping lithium metal within anode-free full and half cells using LPSC as the SSE. Simple cold pressing of copper foil onto LPSC at 15 MPa and room temperature enables the deposition of large amounts of compact lithium metal (> 5 mAh cm^{-2}) at a current density of 1 mA cm^{-2} during the initial *in situ* plating step. Despite impressive plating performance, we show that anode-free cells are fundamentally more prone to short circuiting than lithium-excess cells. This propensity for short circuiting arises because nonuniform stripping and/or plating lead to local lithium depletion and loss of electrochemically active area toward the end of the stripping step, and oxidation at the remaining lithium regions causes current focusing and void formation. Subsequent plating induces premature short circuiting compared to lithium-excess cells due to the growth of lithium filaments at current constrictions. Interestingly, anode-free full cells exhibited comparable CEs

4

to lithium-excess full cells, suggesting that the capacity retention of anode-free SSBs would be similar to cells with excess lithium if short circuiting could be prevented. These findings show that filament growth/short circuiting due to the nonuniform removal of the last lithium from the interface is the key limiting factor for anode-free sulfide SSBs, and strategies to mitigate this degradation mode could enable high-performance anode-free SSBs. To this end, we investigated how preventing localized lithium depletion by retaining a lithium film at the interface can greatly improve the cycling stability of anode-free SSB cells.

2. Results and Discussion

We first studied the initial electrodeposition behavior of lithium metal in anode-free Cu/LPSC/Li half cells. In these half cells, a 10 μm copper foil current collector was cold pressed onto one side of a dense LPSC layer at ~15 MPa of stack pressure. A thick lithium metal foil (~0.3 mm) was simultaneously pressed onto the other side of the LPSC to serve as the lithium source. Figure 1b shows a typical voltage profile when depositing lithium metal onto copper foil at 1 mA cm^{-2}. A nucleation overpotential associated with the initial formation of the lithium metal layer was observed at the beginning of deposition, and the voltage then stabilized to -50 mV. Figure S1 shows magnified views of the nucleation overpotential at different current densities; the overpotential was consistently observed in these cells during initial lithium nucleation and is not a short circuit. Notably, this cell (Figure 1b) was able to plate over 6.5 mAh cm^{-2} before a short circuit occurred, as indicated by the sudden step in the voltage. Electrochemical impedance spectroscopy (EIS) measurements recorded throughout the deposition showed that the assembled cell initially had a very large impedance, which rapidly decreased to a total impedance of ~45 Ω cm^2 after nucleating lithium metal before transitioning into different stages of short circuiting (Figure S2).
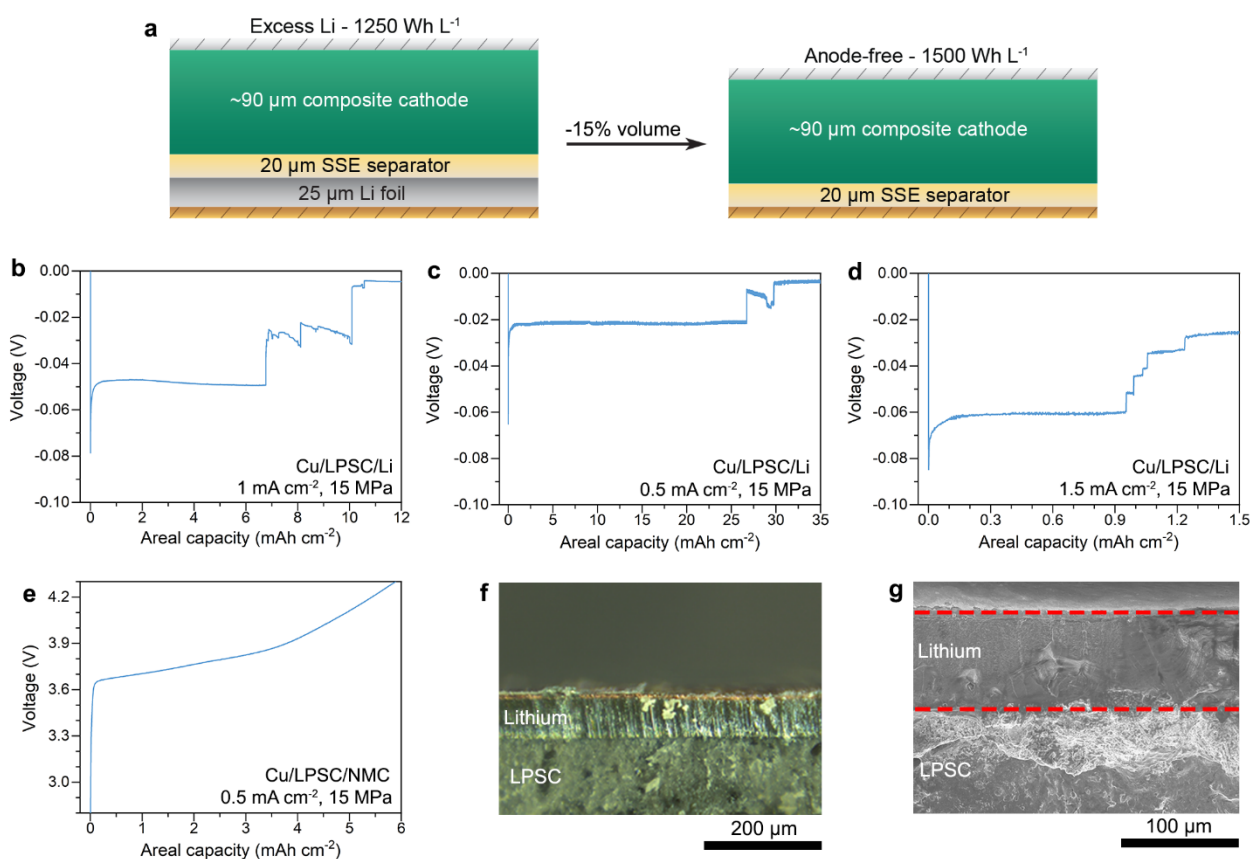
Figure 1. a) Transitioning from using an excess lithium foil as the anode (left) to an anode-free configuration (right) would reduce the stack volume by ~15% and increase energy density. **b)** Depositing lithium metal onto copper foil at 1 mA cm^{-2} in an anode free Cu/LPSC/Li half cell with a stack pressure of 15 MPa. **c)** Depositing lithium metal onto copper foil at 0.5 mA cm^{-2} and 15 MPa. **d)** Depositing lithium metal onto copper foil at 1.5 mA cm^{-2} and 15 MPa. **e)** Charging an anode-free Cu/LPSC/NMC full cell with a cathode loading of 6 mAh cm^{-2} at 0.5 mA cm^{-2} and 15 MPa. **f, g)** Optical and SEM images of thick lithium layers deposited at 0.5 mA cm^{-2} in half cells.

Additional experiments were conducted to understand how lithium deposition is impacted by different cell conditions. Figures 1c, d show the voltage profiles for deposition at current densities of 0.5 mA cm^{-2} and 1.5 mA cm^{-2}, respectively. Over 25 mAh cm^{-2} (125+ μm of lithium) was plated at 0.5 mA cm^{-2}, whereas only 1 mAh cm^{-2} was possible at 1.5 mA cm^{-2} before short circuiting. This behavior is similar to symmetric cells with thick lithium foil electrodes, where the current density plays a key role in how much lithium capacity can be passed before a short circuit forms.[21] Figure 1e shows that *in situ* lithium deposition was also possible in anode-free full cells where the lithium was initially stored in the LiNi$_{0.6}$Mn$_{0.2}$Co$_{0.2}$O$_2$ (NMC) composite cathode. In this cell, nearly all of the 6 mAh cm^{-2} cathode loading was

utilized when charging at 0.5 mA cm^{-2}, demonstrating that large amounts of lithium could be accessed even with thick cathodes.

Stack pressure was found to impact anode-free deposition behavior (Figure S3). Plating at a current density of 1 mA cm^{-2} and a lower stack pressure of 6 MPa yielded slightly less capacity before shorting compared to Figure 1b. This cell also exhibited greater voltage polarization, suggesting that voids could be forming at the stripping interface due to the lower stack pressure. Interestingly, the higher stack pressure of 40 MPa resulted in even lower deposited lithium capacities before short circuiting, despite larger stack pressures typically enhancing interfacial contact. We speculate that this could be due to deformation of the deposited lithium into porosity within the SSE, creating regions with higher effective current densities.[21,34] These findings indicate that future studies are needed to thoroughly assess the effects of stack pressure on anode-free deposition behavior.

Optical microscopy and scanning electron microscopy (SEM) were used to image cross-sections of samples that had thick lithium layers deposited *in situ* at 0.5 mA cm^{-2} (Figures 1f, g). The optical image in Figure 1f shows a layer with a lustrous silver appearance that is typical for pristine lithium metal, and the SEM image in Figure 1g shows a thick layer of lithium on LPSC. Energy dispersive X-ray spectroscopy (EDS) maps taken of a different SEM cross-section only showed an abundance of oxygen in the deposited layer (Figure S4), consistent with the elemental signature of lithium metal that has been briefly oxidized during sample transfer. X-ray photoelectron spectroscopy (XPS) experiments were also conducted on the deposited layer to confirm that the material was lithium metal (Figure S5). The Li 1s and O 1s spectra showed the presence of Li_2O and Li_2O_2 species,[35] which could be explained by lithium metal's surface contamination layer. The absence of peaks in the Cl 2p and P 2p spectra indicated that the Li 1s signal was not from the SSE,[36] which was the only other possible source of lithium in this system. Although the S 2p spectrum exhibited a weak peak, this could possibly be

explained by interactions between the sample and H_2S in the glovebox. Given these combined characterization results, we conclude that the deposited layers are indeed lithium metal.

The ability to deposit > 5 mAh cm^{-2} of lithium at the current density of 1 mA cm^{-2} in half cells is notable given that the cell assembly only used uniaxial cold pressing at moderate stack pressures (15 MPa) to successfully interface copper foil with LPSC. This result contrasts with the challenges of interfacing an anode-free current collector with oxides, such as LLZO, which have required hot pressing at temperatures > 900 °C to form a viable interface.[12] This behavior is likely due to the lower yield strength of sulfides, especially compared to the hard and brittle nature of oxides like LLZO.[37,38] The ability of the SSE to locally deform to contact the current collector is an important factor in developing high-performance anode-free SSBs. We note that in contrast to LLZO, LPSC is not thermodynamically stable in contact with lithium, although the interphase layer only grows to be ~250 nm thick.[39] Interphase formation likely occurs during the first deposition herein but does not appear to detrimentally influence cycling compared to prior work on LLZO.[12]

Cryogenic focused-ion beam (cryo-FIB) milling and SEM imaging were carried out to observe how the thickness and morphology of lithium varied at different locations across the interface after deposition. These experiments leveraged two important capabilities to provide detailed information about the deposition process. First, the anode-free architecture facilitated FIB milling through the entirety of the lithium deposit due to the thinness of the copper foil current collector (~10 μm). Second, milling at cryogenic temperatures was critical to prevent detrimental interactions of the lithium with the gallium beam and the LPSC, as demonstrated by control experiments at different temperatures shown in Figure S6.

Figure 2a-f shows SEM images taken after cryo-FIB milling at different positions on three different electrode samples. The first sample (Figure 2a, b) was extracted from a Cu/LPSC/Li half cell after depositing 3 mAh cm^{-2} of lithium (~15 μm) at a current density of 0.5 mA cm^{-2}. The two images show the Cu/Li/LPSC cross-section near the center (Figure 2a)

and edge (Figure 2b) of the electrode. In each image, the top layer (brighter contrast) is the copper foil. Below that is the deposited lithium (darkest contrast) and then the LPSC electrolyte (intermediate contrast). SEM images from additional trenches on this sample are shown in Figure S7. The lithium deposits in each image were ~15 μm thick regardless of the location on the sample, as expected based on the areal capacity that was plated. The lithium layer thus exhibited highly uniform thickness across the interface when plated at this current density (0.5 mA cm^{-2}), which is similar to results reported by Wang *et al.* at anode-free interfaces using the LLZO SSE.[12] We note that these experiments only provide a handful of randomly-selected local snapshots of the lithium thickness, and that greater variation may not be captured here.
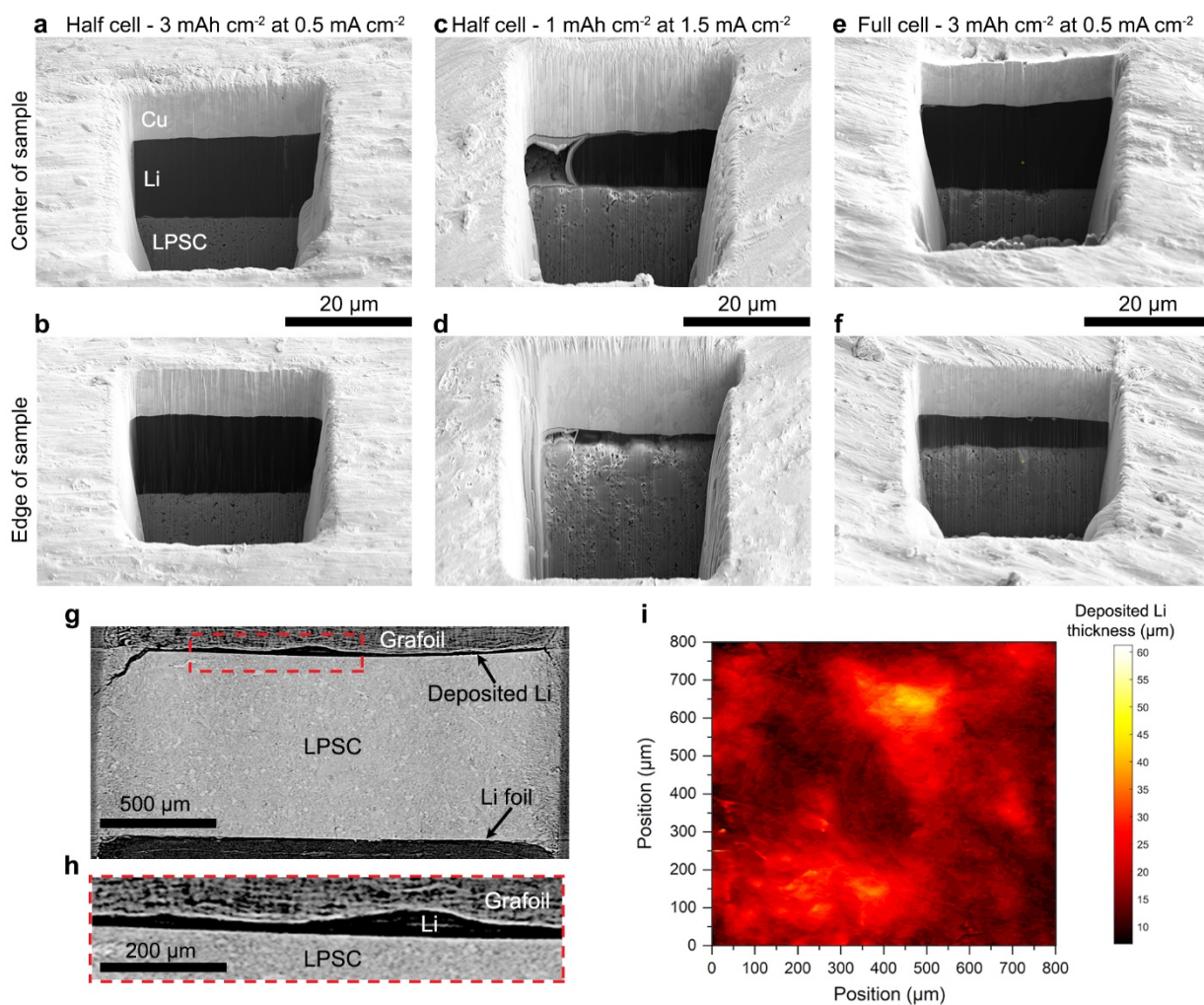
Figure 2. **(a-f)** SEM images taken after cryo-FIB milling through anode-free Cu/LPSC interfaces after lithium deposition. Images in the top row were taken near the center of each electrode sample, while the images in the bottom row were taken near the edge of the electrode. **a, b)** 3 mAh cm^{-2} of lithium deposited at 0.5 mA cm^{-2} in a Cu/LPSC/Li half cell. **c, d)** 1 mAh cm^{-2} deposited at 1.5 mA cm^{-2} in a Cu/LPSC/Li half cell. **e, f)** 3 mAh cm^{-2} deposited at 0.5 mA cm^{-2} in a Cu/LPSC/NMC full cell. **g)** Reconstructed image slice taken from a synchrotron X-ray tomography scan of an anode-free half-cell after ~5.5 mAh cm^{-2} of lithium was deposited at 0.5 mA cm^{-2}. Grafoil was used as the deposition substrate due to the strong X-ray absorption of conventional current collectors like copper and steel, and the tomography cell featured a smaller diameter than cells used for other experiments herein. **h)** Magnified view of the deposited lithium showing variation of lithium thickness across the interface. **i)** Map of the deposited lithium thickness over an 800 μm by 800 μm area of the interface. Brighter colors represent regions with thicker lithium.

The same cryo-FIB/SEM experiment was repeated for a half cell where 1 mAh cm^{-2} of lithium was deposited at the higher current density of 1.5 mA cm^{-2}. Two images from the center and edge are shown in Figure 2c, d. The region at the center of the sample (Figure 2c) had a lithium thickness of 11 μm, exceeding the 5 μm that would be expected if deposition was ideally a

uniform. In contrast, a region at the edge of the electrode sample (Figure 2d) had a lithium thickness of only 2 μm. These results demonstrate that higher current densities can cause lithium to deposit with varying thickness across the electrode surface. This behavior could explain why much less capacity could be plated at 1.5 mA cm^{-2} before shorting compared to 0.5 mA cm^{-2} (Figure 1c, d). Deposition uniformity was also investigated for anode-free full cells. A Cu/LPSC/NMC full cell with a 3 mAh cm^{-2} cathode loading was charged with a current density of 0.5 mA cm^{-2} (Figure 2e, f). The lithium thickness near the center of the sample was 17 μm, while an image taken near the sample's edge showed a much smaller lithium thickness of 6 μm. Given these results, the full cell exhibited lower deposition uniformity compared to the half cell (Figure 2a, b) despite using the same areal capacity and current density. The reasons for these important differences in deposition uniformity are not entirely clear, and it is possible that different distribution of local stress due to the lack of a deformable lithium counter electrode in the full cell could play a role.

Cryo-FIB enables effective imaging of the deposited lithium metal, but this technique is limited by the relatively small size of the milled trenches (~30 μm by 30 μm in this study). To better understand the nature of lithium deposition across much larger interfacial regions, we leveraged synchrotron X-ray tomography to image an entire anode-free SSB after plating (see Methods for details). Figure 2g shows a reconstructed image slice collected from an X-ray tomography scan of an anode-free half cell after ~5.5 mAh cm^{-2} lithium was deposited at 0.5 mA cm^{-2}. Grafoil, a commercial carbon-based conductive foil, was used as the current collector due to the strong X-ray absorption of metal current collectors like copper and stainless steel that preclude effective imaging of the interface. Although Grafoil is comprised of graphitic carbon that could possibly undergo Li intercalation, the galvanostatic electrochemical profile from this cell showed that negligible intercalation occurred, and the cell exhibited the typical nucleation overpotential and voltage plateau expected when depositing lithium (Figure S8). Additionally, the deposited lithium layer was clearly detected at the Grafoil/LPSC interface in Figure 2g-h.

The reconstructed image slices in Figure 2g-h demonstrate that the thickness of the deposited lithium layer varies substantially. While the theoretical thickness value based on the amount of lithium deposited is ~25 µm, the magnified image of the interface (Figure 2h) shows that the lithium thickness varies from approximately 40 µm at its thickest point to 14 µm in the thinnest region. This thickness variation was not attributed to the grafoil, since a pristine cell with a grafoil substrate had a flat interface with the SSE before deposition (Figure S9). Figure 2i shows a two-dimensional map of the lithium thickness as a function of position over an area of 800 µm by 800 µm at the center of the sample, with brighter colors representing regions with thicker lithium. The thickest lithium region is ~50 µm, while the thinnest is below 10 µm. Interestingly, the regions of greater thickness span hundreds of microns, indicating that locally higher current densities existed over relatively large areas. It is important to note that the X-ray tomography results should not be directly compared to the cryo-FIB data in Figure 2a-f, as the tomography experiments used smaller cell housings and smaller electrodes (see Methods), resulting in less uniformity of lithium thickness at the same current density. Overall, however, the results in Figure 2 show that despite the ability to deposit relatively large amounts of lithium onto current collectors, lithium can grow with nonuniform thickness at higher current densities. This finding is important because nonuniform lithium thickness can have consequences during stripping, as explored next.

With an improved understanding of plating at anode-free LPSC interfaces, we next investigated how stripping impacts cell cycling. Figure 3a shows the typical behavior of an anode-free half cell cycled at 0.5 mA cm^{-2} with 3 mAh cm^{-2} capacity deposited per half cycle; this cell short circuited in the third deposition cycle, and other identical cells showed similar rapid short circuiting. The cumulative lithium capacity plated at the Cu/LPSC interface in Figure 3a was 6.5 mAh cm^{-2} (~32 µm total), which is far less than the 25 mAh cm^{-2} (~125 µm) achieved when plating continuously at the same current density (Figure 1c), indicating that cyclic stripping severely diminishes performance and exacerbates short circuiting. The half cell

in Figure 3a exhibited a CE of 90% on the first cycle, meaning that ~1.5 μm (0.3 mAh cm^{-2}) of lithium was left at the interface after the first stripping. It is notable that the stripping curves from the first and second cycles in Figure 3a both show voltage increases near the end of stripping despite lithium being left at the interface. Such voltage polarization has been shown to be associated with the loss of electrochemically active area at the stripping interface.[15–17]

Figure 3b shows typical cycling behavior of an anode-free full cell operated under the same conditions as the half cell in Figure 3a. Interestingly, the full cell shorted in the ninth cycle instead of the third. The improved cyclability of the full cell over the half cell can partially be explained by the full cell's lower first-cycle CE (80%), indicating that a theoretical lithium thickness of ~2.5 μm (0.5 mAh cm^{-2}) remained at the anode current collector after the first discharge. The low initial CE in the full cell was primarily due to the cathode not reincorporating all the lithium during discharge. Cryo-FIB characterization of an anode-free full cell after the first cycle showed that ~1.5 μm of lithium remained at the interface in the milled region (Figure S10). The discrepancy between the ideal and actual amounts of lithium could be explained by deposition nonuniformity, as well as possible irreversible side reactions with the LPSC that can consume additional lithium. These results suggest that the slightly larger amount of lithium left at the interface after the first cycle in full cells can help mitigate the loss of electrochemically active area and improve cycling, although the beneficial effects of this extra lithium degrade over time since the cell still short circuits after the ninth cycle. A full cell using a thick lithium metal foil (~300 μm) as the anode was assembled and tested under the same conditions for comparison to the anode-free cells to better understand the mechanistic limitations of anode-free interfaces (Figure 3c). Because the amount of lithium transferred per cycle was much lower than the thickness of the lithium foil, this cell always retained thick lithium metal at the anode/LPSC interface. This difference substantially enhanced cell performance, as the thick lithium foil full cell was able to complete over 100 cycles without short circuiting.
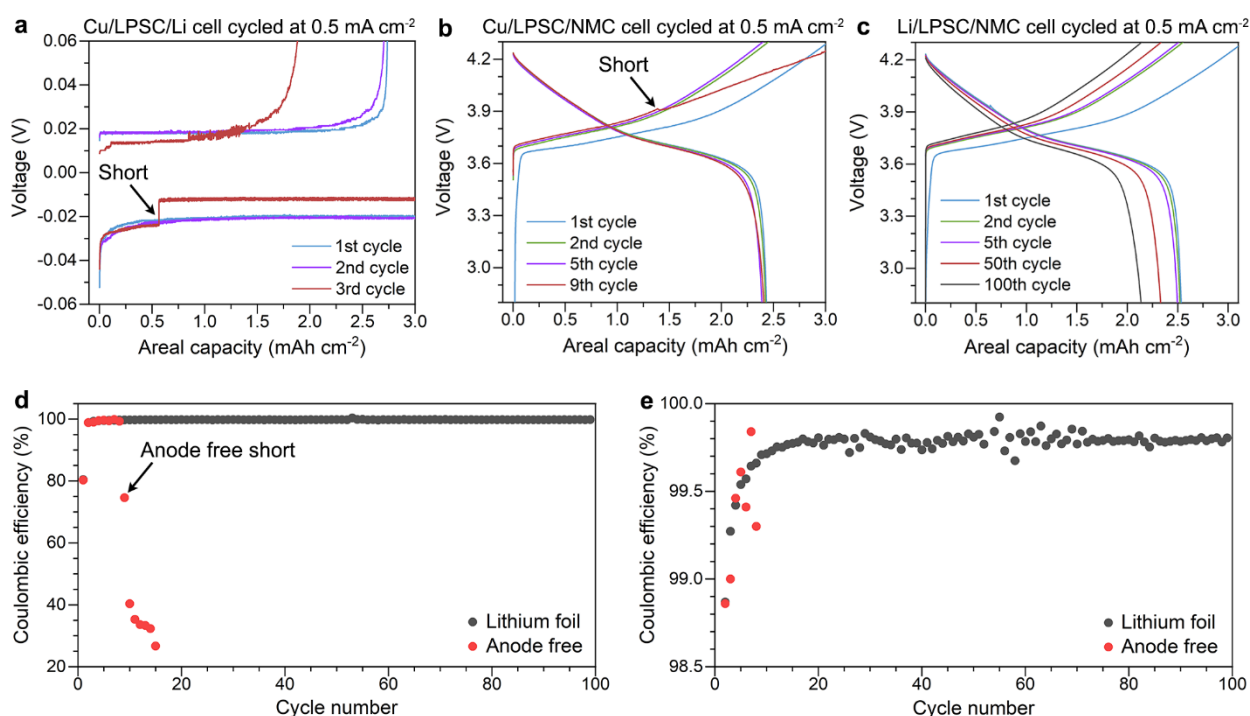
Figure 3. a) Cycling a Cu/LPSC/Li half cell at a current density of 0.5 mA cm^{-2} with a half-cycle capacity of 3 mAh cm^{-2}. **b)** Cycling a Cu/LPSC/NMC full cell at 0.5 mA cm^{-2} with a cathode loading of 3 mAh cm^{-2}. **c)** Cycling a lithium-excess Li/LPSC/NMC full cell at 0.5 mA cm^{-2} with a cathode loading of 3 mAh cm^{-2}. This cell used a lithium metal anode with a thickness of 0.3 mm. **d)** Comparison of the Coulombic efficiencies between the anode-free full cell (red circles) and the full cell with thick lithium foil (black circles). **e)** Magnified view of the plot in **(d)**.

These results show that anode-free cells are fundamentally limited by accelerated short circuiting compared to excess-lithium cells. Interestingly, however, we found that anode-free full cells using LPSC do exhibit high Coulombic efficiency and areal capacity (comparable to lithium-excess cells) before short circuiting. As shown in Figure 3b-c, both types of cells were able to access the total cathode capacity during the first charge, and both exhibited initial CEs of 80%. The CEs of subsequent cycles in the anode-free cell were also similar to the thick lithium foil cell (Figure 3d, e), with the anode-free cell exhibiting an average CE of 99.3% during cycles 2-8 before shorting compared to 99.4% for the thick lithium foil. The excess-lithium full cell showed excellent performance beyond cycle 10 as well, with an average CE of 99.8%. The similar CEs of the two configurations show that the plating and stripping process in the anode-free SSBs are as efficient as in cells with excess lithium.

14

Given these data, we now focus on why anode-free cells exhibit accelerated short circuiting. The underpinning mechanisms that differentiate anode-free SSBs from excess-lithium cells are schematically illustrated in Figure 4a-d. In anode-free cells, lithium is initially deposited onto the current collector and can exhibit nonuniform thickness (Figure 4a), suggesting that the current density can intrinsically vary across the interface. Near the end of the first stripping step (Figure 4b), lithium is completely stripped from some regions of the anode, while some lithium regions remain. This behavior could be caused either by the initial nonuniform thickness of deposited lithium, or by natural variations of current density across the interface. Toward the end of stripping, there will therefore be some regions where lithium has been fully stripped and the SSE is in contact with the current collector ("inactive contact" in Figure 4b), and some regions where lithium remains in contact with the SSE. Physical gaps between the phases could also exist at this point.

We propose that the local depletion of lithium leading to isolated lithium contact regions, as shown in Figure 4b, will play a dominant role in determining the cycling stability and propensity for short circuiting upon further cycling. This is because the formation of isolated lithium regions toward the end of stripping will decrease the electrochemically active area available for stripping, since the inactive Cu/SSE contacts shown in Figure 4b cannot support lithium oxidation. This decrease in electrochemically active interfacial area creates current constrictions at the remaining lithium regions, greatly increasing local current density. At this point, the local stripping current density (j_{strip}) will exceed the critical current density for void formation (j_{void}) at some remaining lithium locations at the interface,[15] and voids will form and accumulate at these isolated lithium regions (Figure 4c). Void formation will further decrease electrochemically active area and will also prevent these regions from being further stripped. This behavior can explain the inability to strip 100% of the deposited lithium in half cells, as demonstrated by the 90% Coulombic efficiency in Figure 3a. Importantly, this behavior is distinct from void formation during stripping in lithium-excess SSBs, since the excess lithium

15

prevents local lithium depletion, with void formation only occurring at relatively high applied current densities. In the anode-free case, the intrinsic current constriction caused by localized lithium depletion will cause voiding even at low applied current densities.

After the stripping step, the current is reversed and plating begins at the interface (Figure 4d). Lithium can be plated at all regions of metallic contact to the SSE, which likely cover a relatively large area of the interface. However, the isolated lithium regions at which voids formed at the end of stripping, as well as any physical gaps at the interface, will tend to cause current constrictions upon plating, which are well known to cause filament growth and short circuiting,[15,17] Some of the voids will be filled upon redeposition, but it only takes a few regions of locally high current density ($j_{plate} > j_{filament}$) to cause filaments to form and grow.
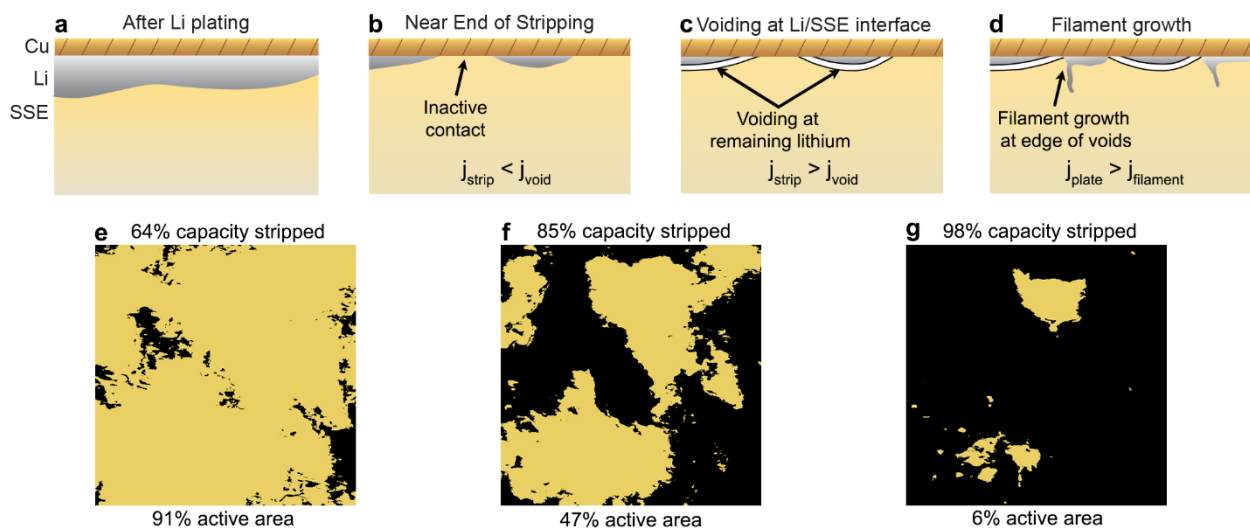

Figure 4. Plating and stripping mechanisms at anode-free interfaces. **a)** Lithium metal is initially deposited onto the current collector and can exhibit nonuniform thickness depending on current density. **b)** During early stripping, the effective current density (j_{strip}) is lower than the critical current density for void formation (j_{void}). After a large fraction of the capacity is stripped, some regions are completely depleted of Li and the electrochemically active area at the interface is reduced. **c)** Continuing to strip after losing active area results in a higher effective j_{strip} that exceeds j_{void} at some remaining lithium regions, leading to the formation of voids. **d)** When plating begins after stripping, current constrictions at the edges of previously-formed voids or gaps can cause local current densities j_{plate} to exceed the critical current density for filament growth, $j_{filament}$, leading to exacerbated filament growth at these locations. **e-g)** Simulated stripping using the synchrotron data in Figure 3c by virtually removing one deposited lithium layer at a time. Black pixels represent regions where lithium has been fully depleted and is no longer present, reducing the electrochemically active area. The percentage of capacity stripped is labeled above each image, while the percentage of active area remaining is labeled below. The edge length of these images is 800 μm.

16

To connect this proposed mechanism to our experimental results, we carried out further analysis of the *ex situ* synchrotron tomography data previously shown in Figure 2. Based on the lithium thickness map in Figure 2i, Figure 4e-g shows snapshots of the electrochemically active area at the interface (i.e., regions of lithium contacting the LPSC) as lithium is stripped at a uniform rate from the interface. In this analysis, we simulated lithium stripping by removing lithium layer-by-layer. Due to the initial thickness variations, loss of electrochemically active area occurs before 100% of the lithium capacity is stripped. Figure 4e shows that 91% of the area is active after stripping 64% of the lithium. Continuing to strip 85% of the total capacity dramatically decreases the active area to 47%, resulting in a current density 2.1 times the nominal value (Figure 4f). In reality, this current density would be even higher in some regions due to current constriction effects. Reduction of electrochemically active area continues as more capacity is stripped, with small isolated regions present near the end of stripping (Figure 4g).

To further investigate this proposed lithium depletion mechanism, we carried out finite element simulations to predict the evolution of voiding behavior at the lithium metal/SSE interface. As detailed in the Methods, SI, and Figure S12, we used a mechanistic phase-field model capable of predicting voiding in the lithium as well as the local current density distribution in the electrolyte during plating/stripping.[42] Figure 5 shows the results of these simulations, with a lithium metal electrode with nonuniform thickness (yellow) in contact with an SSE (blue). This figure shows simulation results at three different times as stripping commences. The normalized current i_l/i_{app} in the SSE is shown by the color gradation scale on the right of Figure 5. The phase field parameter ξ within the lithium, which represents the tendency for voiding (closer to zero represents voiding), is shown by the scale on the left of Figure 5. Shortly after stripping begins (Figure 5a), the current distribution shown in the SSE phase is almost uniform with only slight alteration at the lithium bulge. As stripping proceeds (Figure 5b), the current becomes somewhat localized at the bulge. When the surrounding flat

lithium is completely stripped (Figure 5c), however, the current becomes highly concentrated at the remaining lithium region, inducing obvious voiding at the interface (see inset). This current localization is observed after the loss of surrounding active area, supporting the proposed mechanism.
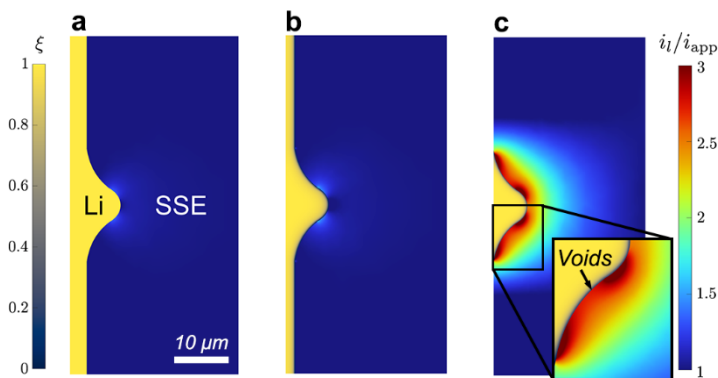

Figure 5. Mechanistic numerical predictions of stripping behavior (as characterized by the phase field parameter ξ within the lithium metal) and normalized current in the SSE i_l/i_{app}, where i_{app} is the globally applied current of 0.25 mA cm^{-2}. **a)** Initial geometry and conditions shortly after stripping begins ($t = 0^+$), with a small lithium bulge introduced to mimic the result of uneven plating/stripping. **b)** Later in the stripping process ($t = 3300$ s), showing some voiding and current localization at the lithium bulge. **c)** Snapshot after the surrounding flat lithium area has been fully stripped ($t = 3800$ s), revealing localized voiding and significant localization of current at the bulge.

These experimental and simulation results show that the plating/stripping mechanisms in anode-free SSBs are fundamentally different from excess-lithium SSBs. The tendency for local lithium depletion and isolated lithium formation during stripping in anode-free SSBs is likely unavoidable since neither deposition nor stripping will always occur with complete uniformity. Thus, the local current density j_{strip} will increase locally and ultimately exceed j_{void} at remaining lithium regions due to the decrease in active area, even for relatively low applied current densities. This differs from lithium-excess SSBs, where there is never local depletion of lithium (i.e., lithium remains present across the entire interface) because of the thick lithium present. Voids can form during stripping in lithium-excess SSBs, but only when the current density is greater than the critical current density for void formation, j_{void}. These concepts explain the improved resistance to short circuiting exhibited by excess-lithium cells (Figure 3c)

compared to the anode-free full and half cells (Figure 3a-b). The requirements for stable operation of anode-free SSBs are thus even more stringent than excess-lithium cells: in addition to preventing general physical contact loss and void formation, lithium must be plated and stripped uniformly across the entire interface to minimize localized lithium depletion.

To better understand these mechanisms, we explored the effects of initially depositing a relatively thick lithium layer and then cycling only a fraction of this layer. Our proposed degradation pathway suggests that this approach should mitigate short circuiting by avoiding local lithium depletion. Figure 6a shows an anode-free half cell operated at 0.5 mA cm^{-2}, where 3 mAh cm^{-2} was deposited initially and then cycled using only half of that capacity (1.5 mAh cm^{-2}). The stripping curves exhibit excellent stability without any voltage polarization over 75 cycles, indicating that the lithium layer was uniformly maintained across the Cu substrate. In addition, no nucleation overpotentials were observed after the initial deposition, which is typical when depositing onto lithium metal[21] and is further evidence for lithium contact retention at the interface. The cell lifetime showed remarkable improvement compared to the case with full stripping (Figure 3a), with a cumulative lithium capacity of ~114 mAh cm^{-2} being deposited onto Cu before a short circuit formed in the 75th cycle (red curve in Figure 6a). A similar experiment (Figure 6b) was conducted using an anode-free full cell with a cathode loading of 3 mAh cm^{-2}, with the cycling capacity controlled to be 1 mAh cm^{-2} after the first charge. This cell also showed improved cyclability compared to the full cell in Figure 3b, lasting over 100 limited cycles without the formation of a short circuit.
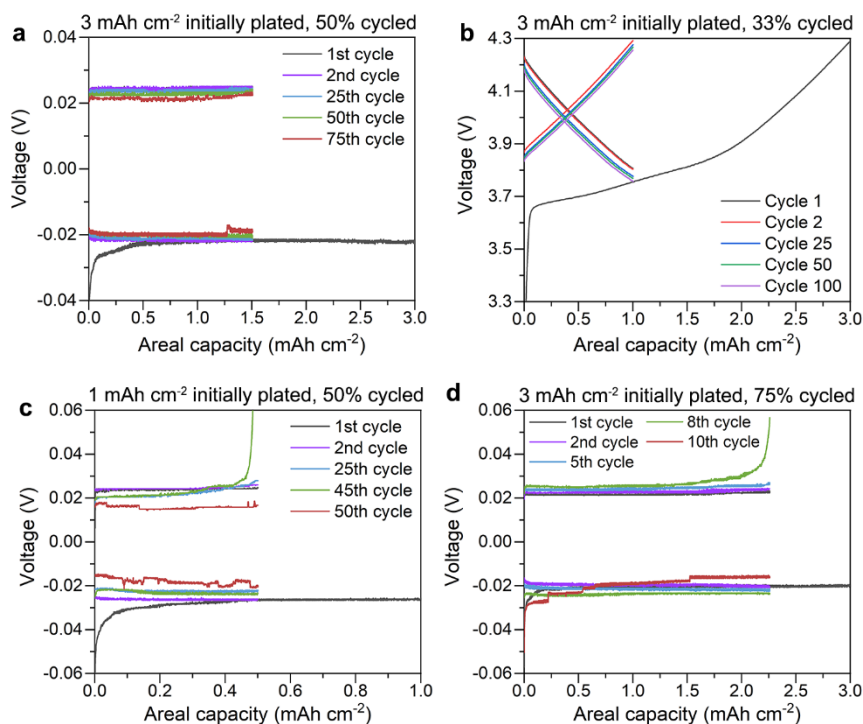
Figure 6. a) Capacity-limited cycling of a Cu/LPSC/Li half cell at 0.5 mA cm^{-2} with an initial deposition step of 3 mAh cm^{-2} and subsequent half cycles controlled to cycle 1.5 mAh cm^{-2}. **b)** Capacity-limited cycling of a Cu/LPSC/NMC full cell with a cathode loading of 3 mAh cm^{-2} and a current density of 0.5 mA cm^{-2}. Each half cycle was controlled to cycle 1 mAh cm^{-2} of capacity after the initial charge. **c)** Limited cycling of a Cu/LPSC/Li half cell at 0.5 mA cm^{-2} with an initial deposition step of 1 mAh cm^{-2} and subsequent half cycles of 0.5 mAh cm^{-2}. **d)** Limited cycling of a Cu/LPSC/Li half cell at 0.5 mA cm^{-2} with an initial deposition step of 3 mAh cm^{-2} and subsequent half cycles of 2.3 mAh cm^{-2}.

An important observation from these limited capacity experiments is that the amount of lithium remaining at the interface strongly impacts cell stability and short circuiting. Figure 6c shows that a half cell that cycled 50% of a lower initial capacity of 1 mAh cm^{-2} short circuited after plating a cumulative capacity of only ~25 mAh cm^{-2} onto Cu, which was much lower than the cell in Figure 6a that had higher initial capacity. Polarization eventually occurred during stripping (see the 45th cycle in Figure 6c), which was likely associated with local lithium depletion and was accompanied by the return of the nucleation overpotential. The reduced lifetime of this cell compared to Figure 6a can be attributed to the thinner amount of lithium left at the interface after stripping (~2.5 μm, 0.5 mAh cm^{-2}), which was less effective in mitigating complete removal of lithium from certain regions of the interface. Similar behavior

was observed with a cell that had a thicker initial layer of 3 mAh cm^{-2} but cycled 75% of the capacity instead of 50% (Figure 6d). Although the initial cycles exhibited stable voltages, the cell began to polarize during the 8th stripping step (green curve), followed by re-nucleation and ultimately short circuiting in the 10th cycle. Like the cell in Figure 6c, less lithium was left at the interface after stripping (~3.75 μm, 0.75 mAh cm^{-2}), making it more likely that some regions would be stripped of lithium entirely and lose active area. These results emphasize the importance of retaining electrochemically active area during stripping at anode-free interfaces.

The cathode loading and initial CE in full cells also play an important role in cycling stability when operating with full depth of discharge. Since the first-cycle CE is much lower than on subsequent cycles, the anode at the end of the first discharge will have remaining lithium metal that is not re-inserted into the cathode (as previously shown in Figure S10). The stranded capacity that remains as lithium metal can be estimated by multiplying the total cathode capacity by the Coulombic inefficiency (*i.e.*, 1-CE), although in reality some of this capacity is consumed by side reactions. Therefore, increasing the cathode loading or decreasing the initial CE should both increase the amount of lithium metal left at the end of the first cycle. To demonstrate the effects of cathode loading, we cycled an anode-free full cell with a cathode areal capacity of 1 mAh cm^{-2} at C/10 (Figure S11). This cell can be compared with the cell in Figure 3b that had a cathode loading of 3 mAh cm^{-2} and cycling rate of C/6. While both cells had similar initial CEs of ~80%, the lower-loading cell exhibited much faster capacity fade, losing 37% of its discharge capacity by the fifth cycle compared to 2% for the higher loading cell. The fifth-cycle charge curve for the lower-loading cell also had high overpotential, which is an indication of more severe local lithium depletion at the end of discharge that results in reduced interfacial area. These results demonstrate that larger cathode loadings can enhance cycling stability due to the greater amount of lithium remaining at the anode after the first cycle.

Strategic electrochemical protocols to carefully control interfacial characteristics, such as those shown in Figure 6, will likely play an important role in the development of anode-free

SSBs. While we have shown the benefits of retaining lithium at the interface by controlling cycle capacity after initial lithium deposition, the protocols demonstrated in Figure 6 are not feasible for commercial batteries because they reduce specific energy and energy density. The cathode loading utilization must be maximized to achieve a high reversible areal capacity and avoid the energy penalty of unused heavy cathode particles. For example, an anode-free cell with a cathode loading of 5 mAh cm^{-2} and 100% capacity utilization would have a stack-level energy density of ~1500 Wh L^{-1} in the discharged state. Decreasing the utilization to 50%, as presented in this work, would reduce the energy density to less than 750 Wh L^{-1} due to reduced capacity utilization and decreased voltage range; this value is only on par with the stack-level energy density of conventional lithium-ion batteries using graphite anodes[41] Thus, although Figure 6 shows the benefits of including extra cathode mass loading for cycling, this is not viable for high-energy SSBs. However, we envision that careful optimization of electrochemical protocols during the end of discharge and at the beginning of charge will be needed to stabilize anode-free cycling while minimizing energy density penalties.

3. Conclusions

This work has demonstrated the feasibility of plating and stripping lithium metal in sulfide-based anode-free SSBs, and through this effort we have revealed degradation mechanisms unique to anode-free SSBs. Using the sulfide SSE Li$_6$PS$_5$Cl, anode-free cells were assembled via simple uniaxial cold pressing at ~15 MPa. Large quantities of lithium (> 5 mAh cm^{-2}) could be plated at room temperature onto the current collector at a relatively high current density of 1 mA cm^{-2} without short circuiting. However, lithium plating and stripping was found to be nonuniform across the interface, causing local depletion of lithium in some regions and decreasing the electrochemically active area. Current constriction effects created by the loss of active area likely increased the stripping current density beyond a critical value to form voids at these remaining lithium regions. These voided lithium regions are highly susceptible to

filament nucleation during subsequent plating steps due to current constriction near the voids. This mechanism is different than that found in lithium-excess SSBs and is expected to be general for any anode-free SSE chemistry. Despite this key limitation, it was shown that anode-free full cells exhibited comparable Coulombic efficiencies to full cells with thick lithium metal foils. In contrast to conventional wisdom, then, it is short circuiting which is the key limitation of anode-free SSBs rather than the minimal lithium inventory.

Our new findings herein provide important guidance for the engineering of anode interfaces for enabling high-performance anode-free SSBs. While Ag-C layers have demonstrated improved cyclability at SSB anode interfaces,[13] engineered solutions that occupy minimal volume and mass are needed to maximize energy density/specific energy. Our results illustrate the importance of mitigating local lithium depletion and the loss of electrochemically active area when fully stripping lithium. Without modifying the interface, it may be unavoidable to form isolated lithium regions at the end of stripping, but careful control of stripping currents and/or voltages could be beneficial for preventing local voiding at these regions. Other solutions that could be effective include interfacial layers that homogenize electrochemical reactions and/or transport at the interface. For instance, interfacial layers that enable Li transport via diffusion to compensate for local lithium depletion could be effective for mitigating current constriction and void formation. Furthermore, inclusion of thin Li foils or other lithium reservoirs could also mitigate local lithium depletion, but would negate some benefits of the "anode-free" architecture.

4. Methods

Materials

Li_6PS_5Cl powder (NEI Corporation) was prepared for use as the SSE separator by hand grinding ~600 mg in a mortar and pestle for ~20 min to reduce the particle size. Copper foil with a thickness of ~10 μm (MTI) was used as the deposition substrate in anode-free cells.

Lithium metal foil (99.9% purity, MSE Supplies) was cleaned before use by rubbing off the surface contamination layer. Composite cathodes were fabricated using a 70:27.5:2.5 weight ratio of single crystal $LiNi_{0.6}Mn_{0.2}Co_{0.2}O_2$ (NMC, MSE Supplies), ultrafine LPSC (MSE Supplies, particle size < 1 μm), and vapor-grown carbon fibers (Sigma Aldrich). To reduce side reactions with LPSC, NMC particles were coated with $LiNb_{0.5}Ta_{0.5}O_3$ (LNTO) following a previously reported procedure.[42,43] The powders were milled together in a planetary ball mill (Fritsch Pulverisette 7) using a zirconia jar with eight 10 mm zirconia balls and ~1 g of composite. A protocol of 10 min of milling at 150 RPM followed by 5 min of rest was applied for 3 cycles to yield the mixed composite cathode.

Assembly and testing of solid-state batteries

SSBs in this study used custom cell housings that were calibrated to apply known amounts of stack pressure by controlling the torque applied to the cell bolts, as based on previous studies.[21,43,44] Anode-free half cells were assembled in an Ar-filled glovebox by first loading 90 mg of ground LPSC into a 10 mm PEEK die and cold pressing in a uniaxial press at 375 MPa for 1 min to form a dense pellet. 10-mm-diameter copper discs were punched out and subsequently cleaned by sonicating in acetone and IPA, followed by blow drying with nitrogen gas. A copper disc was then pressed onto one side of the LPSC pellet using a titanium rod. Lithium metal foil was incorporated by pressing a disc with a thickness of ~0.3 mm onto another titanium rod, cleaning the pressed foil with a toothbrush, and inserting the rod into the die. The entire cell stack was then uniaxially compressed at 15 MPa for 5 min to establish contact at the electrode/SSE interfaces. The cell was then placed between two steel plates and compressed at the desired stack pressure for operation (typically 15 MPa).

Anode-free full cells used a slightly modified assembly procedure. 90 mg of ground LPSC was loaded into the die and compressed by hand to form a compact layer. Composite cathode powder was then poured on top and compressed by hand to form the cathode layer. The

areal capacity loading varied between cells as specified in the text, with 1 mAh cm^{-2} being equivalent to 5.9 mg of composite (assuming a specific capacity of 190 mAh g^{-1}). The cell stack was then cold-pressed uniaxially at 375 MPa for 1 min to densify the layers. Afterwards, a cleaned copper disc was inserted on the anode side of the LPSC layer. The cell was then placed between plates and compressed to a stack pressure of 15 MPa. For full cells using a thick lithium foil instead of an anode-free substrate, lithium metal was incorporated using the same procedure as the anode-free half cells.

Electrochemical experiments were conducted inside an Ar-filled glove box to prevent air exposure. SSBs were tested using a Landt battery cycler or BioLogic SP-200 potentiostat. Electrochemical impedance spectroscopy (EIS) was performed using a frequency range of 2 MHz to 2 Hz and a voltage amplitude of 10 mV. All experiments were performed at room temperature (25 °C).

Characterization

Cryogenic focused ion beam (cryo-FIB) experiments were conducted using a Thermo Fisher Helios 5CX FIB-SEM equipped with a Ga ion source and Quorum cryogenic stage system. Samples were extracted from cells and taken for characterization during the same day. The samples were rapidly transferred into the vacuum chamber, with an air exposure time of ~30 s. We found that the lithium metal layer was not oxidized due to it being confined between the LPSC and copper layers. Before milling, samples were cooled down to -145 °C to reduce detrimental interactions with the ion beam. No protective layers were deposited before milling due to the presence of the copper foil. Initial milling cuts were performed using an ion accelerating voltage of 30 kV and beam current of 45 nA. Final cuts were made at 30 kV and 2.8 nA. Images were collected using an Everhart-Thornley secondary electron detector with an accelerating voltage of 5 kV and current of 0.34 nA.

X-ray tomography scans of anode-free SSBs were collected at the Advanced Photon Source's 2-BM beamline using monochromatic X-rays with an energy of 25.5 keV. 1500 projections were collected over 180° with an exposure time of 400 ms using an optics system consisting of an Oryx 5.0 MP Mono 10GigE detector and a 2× magnification lens. The field of view was ~4.2 by 1.7 mm^2 and the voxel size was 1.7 μm. The anode-free SSB for X-ray tomography was assembled using a specialized cell housing that was smaller than the other housings used herein.[14] This design was chosen to reduce X-ray absorption while maintaining an airtight seal and applying stack pressure. 7 mg of ground LPSC was inserted into the housing and compressed at 225 MPa. A 2 mm disc of Grafoil was placed on one side of the LPSC layer, followed by a 2 mm disc of lithium metal on the other side. Grafoil was chosen as the deposition substrate due to the strong X-ray absorption of metals like copper and stainless steel, which diminishes the ability to resolve lithium metal at the interface. Screws were inserted on each side of the cell and tightened to a torque of 0.1 N-m (corresponding to a stack pressure of ~10 MPa). A MACCOR 4300 battery cycler was used to deposit lithium metal at a current density of 0.5 mA cm^{-2}. TomoPy was used to reconstruct the raw data into images via the GridRec method. Fiji's Trainable Weka Image Segmentation plugin was used to segment the deposited lithium metal in the reconstructed images. The segmented images were then processed in MATLAB to analyze thickness variation across the interface.

Images of the deposited lithium cross-section were collected using both optical microscopy and scanning electron microscopy (SEM). Samples were prepared by depositing lithium metal at 0.5 mA cm^{-2}, extracting from the PEEK die, and cutting the cross-section with a scalpel. This preparation method was observed to introduce some imaging defects, such as vertical streaks in the lithium metal and contamination particles from the SSE (see Figure 1). Optical images were collected using a Keyence VHX-600 digital microscope. SEM images were taken using a Zeiss Ultra 60 SEM with an accelerating voltage of 10 kV.

X-ray photoelectron spectroscopy (XPS) measurements were conducted using a Thermo K-Alpha XPS instrument. The sample was prepared by depositing lithium onto copper at 0.5 mA cm^{-2} in an anode-free half cell for 56 hours. The cell was then disassembled and the lithium layer was removed from the electrolyte and copper foil using a razor. The sample was transferred into the XPS instrument without exposure to ambient air using a vacuum sealed transfer holder. The sample was irradiated with an X-ray beam from an Al Kα source using a 400 μm spot size. The base pressure in the XPS chamber was less than 2.5x10^{-7} mbar and the surface charging effect was compensated with a flood gun with slow electrons and Ar^{+} ions. To minimize the signal from surface contaminants, each spectrum was collected after etching the sample surface with the ion beam for 1140 seconds.

Numerical simulation

The simulation of lithium metal stripping was carried out in the finite element package COMSOL, using the electro-chemo-mechanical phase field-based model by *Zhao et al.*[40] As described in the Supporting Information, the governing equations of the model aim to capture (i) the evolution of voids in the lithium metal anode due to vacancy nucleation and annihilation, (ii) substitutional (bulk and surface) lithium diffusion, (iii) lithium dissolution and deposition at the anode-electrolyte interface, (iv) anode deformation, accounting for creep and lattice distortion, and (v) the current and electric field distribution. As described in the SI, the model parameters were chosen to mimic the conditions of the experiments. The simulated domain has dimensions of 60 μm × 30 μm, with the electrolyte having a width of 27 μm and the anode having a small bulge of 6 μm depth. A total of 318,924 degrees of freedom were used to discretize the model.

Acknowledgements

Conflict of Interest

The authors declare no conflict of interest.

Data Availability Statement

The data that support the findings of this study are available from the corresponding author upon reasonable request. For the purpose of open access, the author has applied a 'Creative Commons Attribution (CC BY)" license to any Author Accepted Manuscript version arising.

Author Contributions

J.A.L. and M.T.M. conceived the study. J.A.L. built the solid-state batteries and tested them. J.A.L. and S.E.S. conducted the cryogenic FIB experiments. Y.L. synthesized and prepared materials for cathodes. J.A.L., S.E.S., and D.L.N. collected the X-ray tomography data. S.G.Y. performed the XPS experiments and analysis. Y.Z. and E.M.-P. conceptualized the model and designed the numerical experiments. R.W. ran the numerical simulations and processed the data. P.S. assisted with the use of beamline 2-BM and reconstruction processing. J.A.L. analyzed the data and wrote the manuscript with M.T.M.

References

[1]   J. Janek, W. G. Zeier, *Nat. Energy* **2016**, 1, 16141.

[2]   Y. Shen, Y. Zhang, S. Han, J. Wang, Z. Peng, L. Chen, *Joule* **2018**, *2*, 1674–1689.

[3]   K. B. Hatzell, X. C. Chen, C. L. Cobb, N. P. Dasgupta, M. B. Dixit, L. E. Marbella, M. T. McDowell, P. P. Mukherjee, A. Verma, V. Viswanathan, A. S. Westover, W. G. Zeier, *ACS Energy Lett.* **2020**, *5,* 922-934.

[4]   P. Albertus, S. Babinec, S. Litzelman, A. Newman, *Nat. Energy* **2018**, *3*, 16–21.

[5]   T. Famprikis, P. Canepa, J. A. Dawson, M. S. Islam, C. Masquelier, *Nat. Mater.* **2019**, *18*, 1278-1291.

[6]   S. Nanda, A. Gupta, A. Manthiram, *Adv. Energy Mater.* **2021**, *11*, 2000804.

[7]   C. Heubner, S. Maletti, H. Auer, J. Hüttl, K. Voigt, O. Lohrberg, K. Nikolowski, M. Partsch, A. Michaelis, *Adv. Funct. Mater.* **2021**, *31*, 2106608.

[8]   A. J. Louli, A. Eldesoky, R. Weber, M. Genovese, M. Coon, J. deGooyer, Z. Deng, R. T. White, J. Lee, T. Rodgers, R. Petibon, S. Hy, S. J. H. Cheng, J. R. Dahn *Nat. Energy* **2020**, *5*, 693–702.

[9]   J. Qian, B. D. Adams, J. Zheng, W. Xu, W. A. Henderson, J. Wang, M. E. Bowden, S. Xu, J. Hu, J.-G. Zhang, *Adv. Funct. Mater.* **2016**, *26*, 7094–7102.

[10]   R. Weber, M. Genovese, A. J. Louli, S. Hames, C. Martin, I. G. Hill, J. R. Dahn, *Nat. Energy* **2019**, *4*, 683–689.

[11]   R. V. Salvatierra, W. Chen, J. M. Tour, *Adv. Energy Sustain. Res.* **2021**, *2*, 2000110.

[12]   M. J. Wang, E. Carmona, A. Gupta, P. Albertus, J. Sakamoto, *Nat. Commun.* **2020**, *11*, 5201.

[13]   Y.-G. Lee, S. Fujiki, C. Jung, N. Suzuki, N. Yashiro, R. Omoda, D.-S. Ko, T. Shiratsuchi, T. Sugimoto, S. Ryu, J. H. Ku, T. Watanabe, Y. Park, Y. Aihara, D. Im, I. T. Han, *Nat. Energy* **2020**, *5*, 299–308.

[14]   J. A. Lewis, F. J. Q. Cortes, Y. Liu, J. C. Miers, A. Verma, B. S. Vishnugopi, J. Tippens, D. Prakash, T. S. Marchese, S. Y. Han, C. Lee, P. P. Shetty, H.-W. Lee, P. Shevchenko, F. De Carlo, C. Saldana, P. P. Mukherjee, M. T. McDowell *Nat. Mater.* **2021**, *20*, 503–510.

[15] J. Kasemchainan, S. Zekoll, D. S. Jolly, Z. Ning, G. O. Hartley, J. Marrow, P. G. Bruce, *Nat. Mater.* **2019**, *18*, 1105-1111.

[16] M. J. Wang, R. Choudhury, J. Sakamoto, *Joule* **2019**, *3*, 2165-2178.

[17] T. Krauskopf, H. Hartmann, W. G. Zeier, J. Janek, *ACS Appl. Mater. Interfaces* **2019**, *11*, 14463–14477.

[18] E. J. Cheng, A. Sharafi, J. Sakamoto, *Electrochim. Acta* **2017**, *223*, 85–91.

[19] L. Porz, T. Swamy, B. W. Sheldon, D. Rettenwander, T. Frömling, H. L. Thaman, S. Berendts, R. Uecker, W. C. Carter, Y.-M. Chiang, *Adv. Energy Mater.* **2017**, *7*, 1701003.

[20] E. Kazyak, R. Garcia-Mendez, W. S. LePage, A. Sharafi, A. L. Davis, A. J. Sanchez, K.-H. Chen, C. Haslam, J. Sakamoto, N. P. Dasgupta, *Matter* **2020**, *2*, 1025-1048.

[21] J. A. Lewis, C. Lee, Y. Liu, S. Y. Han, D. Prakash, E. J. Klein, H.-W. Lee, M. T. McDowell, *ACS Appl. Mater. Interfaces* **2022**, *14*, 4051–4060.

[22] Z. Ning, D. S. Jolly, G. Li, R. De Meyere, S. D. Pu, Y. Chen, J. Kasemchainan, J. Ihli, C. Gong, B. Liu, D. L. R. Melvin, A. Bonnin, O. Magdysyuk, P. Adamson, G. O. Hartley, C. W. Monroe, T. J. Marrow, P. G. Bruce, *Nat. Mater.* **2021**, *20*, 1121-1129.

[23] G. M. Hobold, J. Lopez, R. Guo, N. Minafra, A. Banerjee, Y. S. Meng, Y. Shao-Horn, B. M. Gallant. *Nat. Energy* **2021**, *6*, 951–960.

[24] J. Xiao, Q. Li, Y. Bi, M. Cai, B. Dunn, T. Glossmann, J. Liu, T. Osaka, R. Sugiura, B. Wu, J. Yang, J-G. Zhang, M. S. Whittingham, *Nat. Energy* **2020**, *5*, 561–568.

[25] X. Fan, X. Ji, F. Han, J. Yue, J. Chen, L. Chen, T. Deng, J. Jiang, C. Wang, *Sci. Adv.* **2018**, *4*, eaau924.

[26] X. Ji, S. Hou, P. Wang, X. He, N. Piao, J. Chen, X. Fan, C. Wang, *Adv. Mater.* **2020**, *32*, 2002741.

[27] M. J. Lee, J. Han, K. Lee, Y. J. Lee, B. G. Kim, K.-N. Jung, B. J. Kim, S. W. Lee, *Nature* **2022**, *601*, 217–222.

[28] T. Krauskopf, R. Dippel, H. Hartmann, K. Peppler, B. Mogwitz, F. H. Richter, W. G. Zeier, J. Janek, *Joule* **2019**, *3*, 2030-2049.

[29] A. L. Davis, E. Kazyak, D. W. Liao, K. N. Wood, N. P. Dasgupta, *J. Electrochem. Soc.* **2021**, *168*, 070557.

[30] M. Motoyama, M. Ejiri, Y. Iriyama, *J. Electrochem. Soc.* **2015**, *162*, A7067.

[31] F. J. Q. Cortes, J. A. Lewis, J. Tippens, T. S. Marchese, M. T. McDowell, *J. Electrochem. Soc.* **2020**, *167*, 050502.

[32] S. Kim, C. Jung, H. Kim, K. E. Thomas-Alyea, G. Yoon, B. Kim, M. E. Badding, Z. Song, J. Chang, J. Kim, D. Im, K. Kang, *Adv. Energy Mater.* **2020**, *10*, 1903993.

[33] K. Lee, E. Kazyak, M. J. Wang, N. P. Dasgupta, J. Sakamoto, *Joule* **2022**, *6*, 2547-2565.

[34] J.-M. Doux, H. Nguyen, D. H. S. Tan, A. Banerjee, X. Wang, E. A. Wu, C. Jo, H. Yang, Y. S. Meng. *Adv. Energy Mater.* **2020**, *10*, 1903253.

[35] K. N. Wood, G. Teeter, *ACS Appl. Energy Mater.* **2018**, *1*, 4493-4504.

[36] S. Wenzel, S. J. Sedlmaier, C. Dietrich, W. G. Zeier, J. Janek, *Solid State Ion.* **2018**, *318*, 102-112.

[37] C. E. Athanasiou, X. Liu, M. Y. Jin, E. Nimon, S. Visco, C. Lee, M. Park, J. Yun, N. P. Padture, H. Gao, B. W. Sheldon, *Cell Rep. Phys. Sci.* **2022**, *3*, 100845.

[38] M. Papakyriakou, Y. Liu, Z. Liu, H. Chen, M. T. McDowell, S. Xia, *J. Power Sources* **2021**, *516*, 230672.

[39] S.-K. Otto, J. M. Riegger, T. Fuchs, S. Kayser, P. Schweitzer, S. Burkhardt, A. Henss, J. Janek, *Adv. Mater. Interfaces* **2022**, *9*, 2102387.

[40] Y. Zhao, R. Wang, R., E. Martínez-Pañeda, *J. Mech. Phys. Solids* **2022**, *167*, 104999.

[41] J. A. Lewis, K. A. Cavallaro, Y. Liu, M. T. McDowell, *Joule* **2022**, *6*, 1418-1430.

[42]   W. Zhang, D. A. Weber, H. Weigand, T. Arlt, I. Manke, D. Schröder, R. Koerver, T. Leichtweiss, P. Hartmann, W. G. Zeier, J. Janek, *ACS Appl. Mater. Interfaces* **2017**, *9*, 17835–17845.

[43]   S. Y. Han, C. Lee, J. A. Lewis, D. Yeh, Y. Liu, H.-W. Lee, M. T. McDowell, *Joule* **2021**, *5*, 2450-2465.

[44]   C. Lee, S. Y. Han, J. A. Lewis, P. P. Shetty, D. Yeh, Y. Liu, E. Klein, H.-W. Lee, M. T. McDowell, *ACS Energy Lett.* **2021**, *6*, 3261–3269.